

Molecular-dynamics investigation of the simple droplet critical wetting behavior at a stripe pillar edge defect

Xiaolong Liu(刘小龙), Chengyun Hong(洪成允), Yong Ding(丁勇), Xuepeng Liu(刘雪朋), Jianxi Yao(姚建曦), Songyuan Dai(戴松元)

Citation: Chin. Phys. B . 2019, 28(1): 014703. **doi:** 10.1088/1674-1056/28/1/014703
Journal homepage: http://cpb.iphy.ac.cn; http://iopscience.iop.org/cpb

What follows is a list of articles you may be interested in

Phase field simulation of single bubble behavior under an electric field

Chang-Sheng Zhu(朱昶胜), Dan Han(韩丹), Sheng Xu(徐升)

Chin. Phys. B . 2018, 27(9): 094704. **doi:** 10.1088/1674-1056/27/9/094704

Physical and chemical effects of phosphorus-containing compounds on laminar premixed flame

Yongfeng Yin(殷永丰), Yong Jiang(蒋勇), Rong Qiu(邱榕), Caiyi Xiong(熊才溢)

Chin. Phys. B . 2018, 27(9): 094701. **doi:** 10.1088/1674-1056/27/9/094701

A multicomponent multiphase lattice Boltzmann model with large liquid-gas density ratios for simulations of wetting phenomena

Qing-Yu Zhang(张庆宇), Dong-Ke Sun(孙东科), Ming-Fang Zhu(朱鸣芳)

Chin. Phys. B . 2017, 26(8): 084701. **doi:** 10.1088/1674-1056/26/8/084701

Turbulence modulation model for gas-particle flow based on probability density function approach

Lu Wang(王路), Jiang-rong Xu(徐江荣)

Chin. Phys. B . 2017, 26(8): 084702. **doi:** 10.1088/1674-1056/26/8/084702

Gradient-augmented hybrid interface capturing method for incompressible two-phase flow

Zheng Fu(付峥), Shi-Yu Wu(吴士玉), Kai-Xin Liu(刘凯欣)

Chin. Phys. B . 2016, 25(6): 064701. **doi:** 10.1088/1674-1056/25/6/064701

Molecular-dynamics investigation of the simple droplet critical wetting behavior at a stripe pillar edge defect*

Xiaolong Liu(刘小龙)[1,2,†], Chengyun Hong(洪成允)[2], Yong Ding(丁勇)[1,2], Xuepeng Liu(刘雪朋)[1,2], Jianxi Yao(姚建曦)[1,2], and Songyuan Dai(戴松元)[1,2,‡]

[1] *Beijing Key Laboratory of Novel Thin-Film Solar Cells & Beijing Key Laboratory of Energy Safety and Clean Utilization, North China Electric Power University, Beijing* 102206, *China*

[2] *Renewable Energy School, North China Electric Power University, Beijing* 102206, *China*

(Received 20 September 2018; revised manuscript received 7 November 2018; published online 12 December 2018)

The microscopic stripe pillar is one of the most frequently adopted building blocks for hydrophobic substrates. However, at high temperatures the particles on the droplet surface readily evaporate and re-condense on the pillar sidewall, which makes the droplet highly unstable and undermines the overall hydrophobic performance of the pillar. In this work, molecular dynamics (MD) simulation of the simple liquid at a single stripe pillar edge defect is performed to characterize the droplet's critical wetting properties considering the evaporation–condensation effect. From the simulation results, the droplets slide down from the edge defect with a volume smaller than the critical value, which is attributed to the existence of the wetting layer on the stripe pillar sidewall. Besides, the analytical study of the pillar sidewall and wetting layer potential field distribution manifests the relation between the simulation parameters and the degree of the droplet pre-wetting, which agrees well with the MD simulation results.

Keywords: molecular-dynamics simulation, simple liquid, single stripe, critical wetting

PACS: 47.11.–j, 47.11.Mn, 47.10.Fg **DOI:** 10.1088/1674-1056/28/1/014703

1. Introduction

On well-fabricated self-cleaning substrates, droplets roll off at a small substrate tilt angle or bounce up easily when dropping on the substrates. The self-cleaning property is usually termed as superhydrophobicity, the researches on which have been focusing on various aspects, including the liquid wetting behaviors on chemically or topologically modified substrates,[1,2] the droplet contact angle (CA) advancing and receding,[3,4] the biomimetic fulfilment of the lotus-leaf effect via various novel surface roughing techniques,[5,6] and so on. One of the most widely adopted superhydrophobic substrates is the periodic microscopic stripe pillar array. Numerous experimental studies and computer-assisted simulations have investigated the relation between the pillar repeating mode and the droplet repellency.[7,8] What is more, it is revealed that the surface modification (physically roughing or chemically decorating) of individual pillar top facets and sidewalls efficiently improves the pillar array's superhydrophobicity.[5,9]

There are two requirements that superhydrophobic substrates should satisfy: the droplet CA should be larger than 150° in general;[1] and the difference between the advancing CA and the receding CA, i.e. CA hysteresis, should be small. On pillar array substrates, generally, droplets are in two states: the Cassie state[11], and the Wenzel state.[12] The droplet CA is smaller for the Wenzel state, and CA hysteresis in the Wenzel state is larger than that in the Cassie state. There exists an apparent Gibbs pinning energy for the Cassie–Wenzel state transition,[13] and once the Wenzel state is approached, the droplet rolling off on the pillar array is prohibited since the droplet adheres to the substrate bottom rather than the pillar top.[14,15]

At high temperatures, the particles on the droplet surface evaporate and then re-condense on the pillar sidewalls, which lowers the Cassie–Wenzel state transition energy barrier,[15,16] resulting in the Wenzel state prevailing, and undermining the self-cleaning performance of the pillar array. Therefore, it is necessary to explore the droplet vapor–liquid–solid triple-phase contact line (TPL) deforming behavior at the pillar edges during the Cassie–Wenzel state transition process in a more detailed way taking the droplet evaporation effect into consideration. As the first step, we explore the droplet critical wetting behavior at the edge defect of a single stripe pillar by molecular dynamics (MD) simulation, and the droplet evaporation effect is included by adopting the Lennard–Jones (LJ) droplet (simple liquid) as the research candidate, with the particles on the droplet surface unstable above the evaporation temperature.

Specifically, the droplet critical wetting behavior is where the droplet TPL will deform and cross over the pillar edge defect to wet the pillar sidewall at a certain critical droplet

*Project supported by the National Key Research and Development Program of China (Grant No. 2016YFA0202401), the National Natural Science Foundation of China (Grant No. 61705066), and the Fundamental Research Funds for the Central Universities, China (Grant No. 2017MS028).

†Corresponding author. E-mail: xl.liu@ncepu.edu.cn

‡Corresponding author. E-mail: sydai@ncepu.edu.cn

© 2019 Chinese Physical Society and IOP Publishing Ltd

size V_c, which has been explored experimentally with different kinds of liquids by increasing the droplet volume through a center hole drilled in the pillar.[17] Correspondingly, the critical wetting angle θ_c is depicted in figure 1, which is the acute dihedral angle between the droplet tangential plane and the plane parallel to the pillar sidewall at a certain point of the TPL. The critical wetting angle θ_c equals the droplet equilibrium CA θ_e on the planar substrates with the same surface properties as the pillar sidewall, and this equivalence relation was first discussed geometrically by Gibbs.[18]

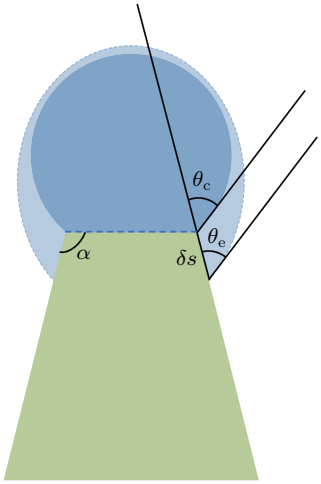


Fig. 1. Side view of a schematic representation of the droplet critical wetting process on a single stripe pillar.

In Fig. 1, α is the angle between the pillar top facet and pillar sidewalls, which indicates the pillar sharpness (a sharper pillar corresponds to a smaller α). In this work, α is 90°, and we believe that the calculations with other pillar tilt angles will lead to the same conclusions.

The equilibrium CA θ_e on the planar substrates can be computed from the extended Young's equation:[19] $\gamma_{LV}\cos\theta_e = \gamma_{SV} - \gamma_{SL} - \tau/r$, where γ_{LV}, γ_{SV}, and γ_{SL} are the liquid–vapor, solid–vapor, and solid–liquid interfacial tensions, respectively, while τ is the line tension of the droplet contact line with $1/r$ as its curvature. Since the curvature of a cylindrical droplet contact line on the stripe pillar is zero, the droplet size effect included in the line tension term is eliminated, and we then use cylindrical droplets to measure θ_e. For the same reason, the droplet on the pillar top is also cylindrical along the y direction (the axes are shown in Fig. 2) for the measurement of the critical wetting angle θ_c. We need to mention that the planar substrates and pillars are infinite along the y direction to support the cylindrical droplets.

Considering that the droplet resting on the soft substrates introduces a complex elastic displacement field,[20] which deforms the TPL and brings uncertainties to the CA measurement, the pinning force calculation would be more complex for the droplets on the flexible pillars.[21] To exclude the TPL deformation effect, the planar substrates and pillars are kept rigid during the MD simulation in this work to avoid influences from the asymmetric strain distribution of the substrates.

In the following, θ_c and θ_e are compared for the droplets with different LJ potential parameters. In this way, the critical wetting properties of the droplets at sharp edge defects are explored.

2. Numerical setup and CA measurement

The width of the stripe pillar is 51 platinum face-centered cubic crystal (fcc) layers, the pillar length is 21 fcc layers, and the height is 20 fcc layers, which is thick enough to avoid the interactions of particles from the vertical neighboring simulation cells. For the same purpose, the thickness of the planar substrate is also 20 fcc layers.

The interactions between all the particles are described by the LJ 12–6 potential

$$\phi(ij) = 4\varepsilon_{ij}\left[\left(\frac{\sigma_{ij}}{r_{ij}}\right)^{12} - \left(\frac{\sigma_{ij}}{r_{ij}}\right)^{6}\right]. \quad (1)$$

Here, i and j stand for the solid, liquid, and vapor particles. Solid–liquid interaction parameters (ε_{SL} and σ_{SL}) are varied to tune the wettability of the substrate, which is represented as different droplet CAs, while the other LJ parameters remain the same during the simulation. For each group of ε_{SL} and σ_{SL}, θ_c and θ_e are compared to test the applicability of the Gibbs critical wetting criterion considering the evaporation effect. The NVT ensemble (particle number, simulation box size, and temperature are fixed) implemented by software LAMMPS[22] is adopted for all simulations. The cutoff radius of the LJ interaction is $2.5\sigma_{LL}$, and the simulation time step is 1.0 femtosecond. All simulations are performed at 100 K, which is above the vaporization temperature although lower than the critical point of the LJ fluid with the given liquid–liquid interaction parameters.

2.1. Equilibrium CA on the planar substrate

All droplets with different LJ solid–liquid parameters are stabilized after 3×10^6 time steps, and then the droplets reach the equilibrium state on the planar substrate. The particle number density field is computed over 1.5–3×10^6 time steps by time and space averaging until the density profile converges. In the computing procedure, the mass centers of the droplets are fixed to accelerate the density profile's convergence.

To measure the equilibrium CA θ_e, we use a circular fit of the droplet Gibbs dividing surface between the liquid and vapor phases[23] at $\rho^* = 0.5$. ρ^* is the post-treated density contour, defined as $\rho^* = \frac{\rho-\rho_V}{\rho_L-\rho_V}$. Here, ρ is the untreated density at a certain point of the density field, while ρ_V and ρ_L are the bulk vapor density and bulk liquid density, respectively. To obtain the measurement deviation, the circular fitting of the

droplet profiles with ρ^* equal to 0.4 and 0.6 is also performed. These three typical density contours are depicted in Fig. 2.

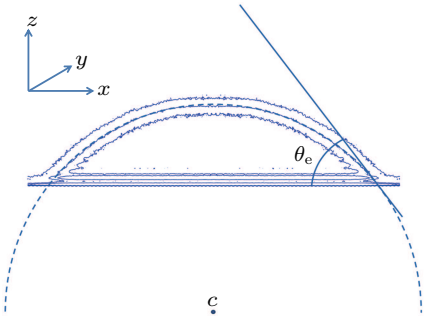


Fig. 2. The ρ^* isodensity contours of the droplet on the planar substrate. From outer to inner, ρ^* equals 0.4, 0.5, and 0.6, respectively.

The liquid density oscillation near the substrate surface results in the droplet layering as depicted in Fig. 2. To measure θ_e, the laying part is ignored, and the circular line is extrapolated to the substrate surface as done in Refs. [23] and [24]. The measurement results of θ_e will be presented in Section 3.

In Fig. 3, the droplet density oscillation pattern along the z direction from the substrate surface is depicted. It is computed by time and space averaging along the cylindrical droplet midline at which the droplet mess center is fixed. From Fig. 3, the bulk liquid density ρ_L is obtained at a height of $7\sigma_{LL}$ (2.38 nm) from the substrate surface along the cylindrical droplet midline, where the droplet density is stabilized. The bulk vapor density ρ_V is obtained away from the droplet.

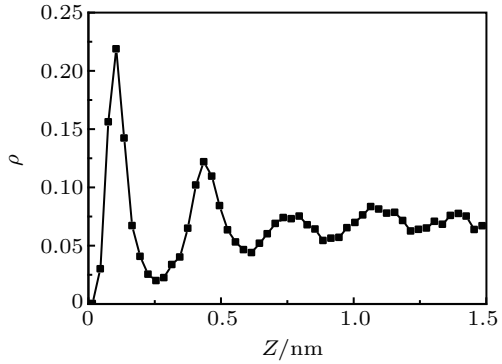


Fig. 3. The density oscillation along the droplet midline as a function of the distance z from the substrate surface.

2.2. Critical wetting angle at the stripe pillar edge defect

To obtain the droplet critical wetting angle θ_c at a stripe pillar edge defect, the droplet is increased by adding particles onto it to approach the critical volume V_c:

$$V_c = \frac{1}{2}\frac{a^2}{\cos^2\theta_c}(\pi + 2\theta_c + \sin 2\theta_c)L, \tag{2}$$

where a is half of the width of the pillar top, L is the length of the pillar along the y axis (which is also the simulation bin size along the y direction, and the three Cartesian axes are shown in Fig. 2).

The particle deposition region is a cuboid and the distance from its lower surface to the droplet top is within the cut-off radius of the LJ interaction ($2.5\sigma_{LL}$). To reduce the artificial disturbance to the minimum, the mass centers of the deposition region and the droplet are set to along the pillar midline and the net vertical velocity of the particles deposited is set to be zero. After 300000–600000 timesteps, the droplet profile is checked. If the droplet slides down to wet the pillar sidewall (Fig. 4(b)), we then redo the deposition process with half the particle number. We need to mention that the depositing particle number in the first trial increases as the droplet equilibrium CA θ_e increases (a large θ_e corresponds to a large droplet critical volume with a small σ_{SL} and small ε_{SL}). One snapshot of the MD evolution after particle deposition is shown in Fig. 4(a).

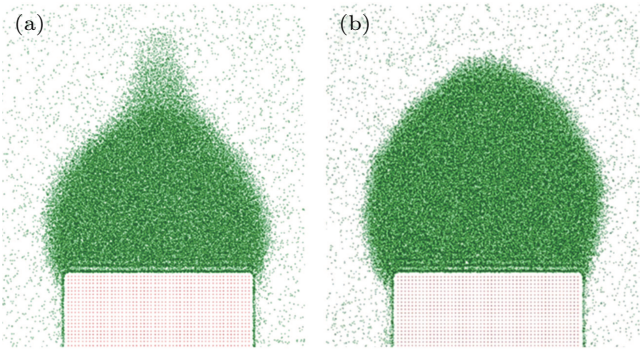


Fig. 4. Snapshots of the particle deposition and the droplet TPL deforming across the pillar edge defect.

Finally, given that the density contour is difficult to converge since the droplet on the pillar top is highly unstable near its critical size, the critical CA θ_c defined in Fig. 1 is obtained by a circular fit of the droplet side view on the xz plane[24] as in Fig. 5. The measurement results of θ_c will be presented together with θ_e in the following section.

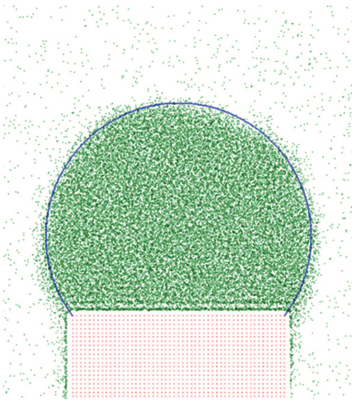


Fig. 5. Circular fitting of the side view of the critical droplet on the stripe pillar top.

3. Results and discussion

The results of the droplet equilibrium CAs θ_e on the planar substrates and the critical wetting angles θ_c at the stripe

pillar edge defects are listed in Table 1 for different LJ solid–liquid interaction parameters.

Table 1. The results of θ_e and θ_c for the LJ liquids with different solid–liquid interaction parameters.

$\sigma_{SL} = 0.9\sigma_{LL}$	$\theta_e/(^\circ)$	$\theta_c/(^\circ)$
$\varepsilon_{SL} = 0.50\varepsilon_{LL}$	52.4± 0.6	44.5
$\varepsilon_{SL} = 0.55\varepsilon_{LL}$	40.5± 0.7	32.5
$\varepsilon_{SL} = 0.60\varepsilon_{LL}$	37.1± 0.5	17.0
$\sigma_{SL} = 0.8\sigma_{LL}$	$\theta_e/(^\circ)$	$\theta_c/(^\circ)$
$\varepsilon_{SL} = 0.60\varepsilon_{LL}$	64.1± 0.3	55.0
$\varepsilon_{SL} = 0.65\varepsilon_{LL}$	57.4± 0.3	45.0
$\varepsilon_{SL} = 0.70\varepsilon_{LL}$	35.1± 0.4	21.0

The measurement accuracies of θ_e and θ_c are chosen as 0.1° and 0.5°, respectively. The different measurement accuracies stem from the fact that the circular fitting of the side view of the cylindrical droplet on the pillar is less accurate than the circular fitting of the droplet isodensity contour on the planar substrate.

From Table 1, for each group of ε_{SL} and σ_{SL}, it is obvious that the critical wetting angle of the LJ liquid droplet is always smaller than the corresponding equilibrium CA. As a result, the droplet TPL will deform and slide down from the pillar edge even when the droplet volume is smaller than the critical value. This phenomenon is termed as pre-wetting here, and for droplets with a smaller θ_e, the pre-wetting phenomenon is more significant according to Table 1. We need to mention that, with the CA approaching 90°, the droplet volume tends to be infinite (as drawn in Fig. 6); for this reason, in this work only the hydrophilic droplets are simulated.

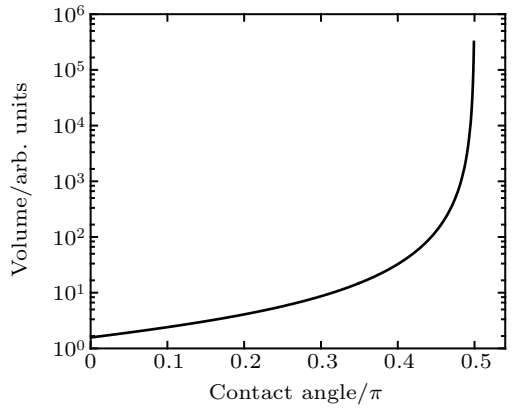


Fig. 6. The dependence of the critical droplet volume on the CA according to Eq. (2) with normalized a and L.

From the work of Mayama,[25] it is suggested that the droplet TPL should overcome a pinning energy barrier E_P at the pillar edge to wet the pillar sidewall. The pinning energy is derived from the free energy minimum difference between two equilibrium states (droplet on the pillar top and droplet wetting of the pillar sidewall), which arises from the droplet shape deformation during the sidewall wetting process. Considering the pinning energy, to wet the pillar sidewall, the droplet volume should be larger than the critical value, i.e. θ_c should be larger than θ_e. Through combining Mayama's formulating and the results in this work together, it is straightforward that the pinning energy barrier at the pillar edge defect for the LJ droplet is lowered, and we attribute it to the moisture layer (ML) effect at the pillar sidewall. The ML here has a similar nature as the precursor layer in Ref. [26]; the formation reason is that the Gibbs free energy of the molecular adhered to the solid surface is lower than that in the gaseous state, which will be discussed in detail in the following sections.

3.1. Atomic explanation of the ML effect

From the side view of the droplet on the stripe pillar top in Fig. 5, we find that the liquid particles wet the pillar sidewall and form a an ML. Besides, the isodensity contour of $\rho^* = 0.4$ of the droplet on the pillar top spreads over the pillar sidewall. Both results prove the existence of the ML on the pillar sidewall, and the underlying reason for this is that the moist sidewall is energetically favorable over the dry sidewall without any particle adsorption.[27] The ML formation has two main resources: one is the direct adsorption of the particles from the gaseous atmosphere, and the other is from the droplet particle evaporation–condensation process near the pillar edge.

The molecular kinetic theory[28] is adopted here to qualitatively explain the pillar pinning energy reduction ΔE_P caused by the ML effect. We define κ_0 as the equilibrium attempting frequency for the droplet particles at the TPL to escape and to be trapped by the ML, and κ_0 is related to the pinning energy barrier E_P, $\kappa_0 \sim \exp\left(\frac{-E_P}{k_B T}\right)$. The existence of the ML on the pillar sidewall greatly enhances κ_0, which indicates that the pinning energy E_P is evidently lowered.

The ML thickness and ML particle density are two key factors for the pinning energy reduction. We need to mention that the ML thickness depends on how to define the ML–vapor interface.

These ML properties are directly related to the sidewall potential field $V(d)$

$$\frac{V(d)}{\nu} = 8\pi\varepsilon_{SL}\left(\frac{1}{3}\frac{\sigma^6}{r_c^3} - \frac{1}{4}\frac{\sigma^6 d}{r_c^4} - \frac{1}{12}\frac{\sigma^6}{d^3} - \frac{1}{9}\frac{\sigma^{12}}{r_c^9} + \frac{1}{10}\frac{\sigma^{12} d}{r_c^{10}} + \frac{1}{90}\frac{\sigma^{12}}{d^9}\right). \quad (3)$$

In Fig. 7, the pillar sidewall potential field is depicted according to Eq. (3). Here, ν is the volume occupied by a single sidewall particle, and σ equals σ_{SL}. At point P, with the distance from the pillar sidewall surface being d, the sidewall potential $V(d)$ is calculated from the integration of the LJ 12–6 potentials of the particles constructing the pillar sidewall within the LJ interaction cutoff radius r_c from P. That is to say, only the portion of the sidewall within the sphere centering at P with the radius of r_c contributes to the calculation of $V(d)$

(i.e. within the arc ABC from the side view on the xz plane in Fig. 7). $V(d)$ tends to be infinite near the sidewall surface and vanishes at P'. The distance from P' to the pillar surface is r_c. After calculation, we know that the first energy valley (and the only one) of $V(d)$ appears at point Q, and the distance from Q to the sidewall surface is

$$d_Q = 0.86\sigma_{SL}. \tag{4}$$

The adsorbed particles on the sidewall would form the first ML with the density peak at d_Q from the sidewall surface, and we take the thickness of the first ML as d_Q.

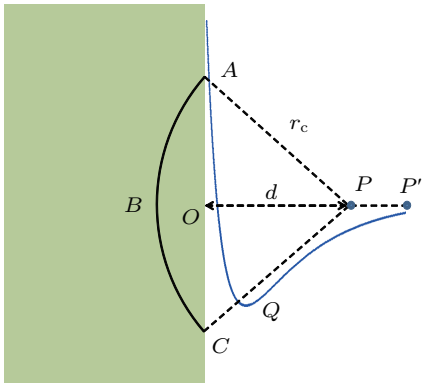


Fig. 7. The pillar sidewall potential field.

However, the ML should be multi-layered. For the second ML, the position of its particle density peak should be determined by both the pillar sidewall potential field and the first ML. We assume that only the particles in the first ML condensed at the distance d_Q from the pillar sidewall have influence on the second ML formation. From Ref. [29], the potential field of the first ML is

$$\phi(Z) = \frac{4\sqrt{3}\pi}{15}\frac{\varepsilon_{LL}{\sigma_{LL}}^2}{\sigma_M^2}\left\{2\left(\frac{\sigma_{LL}}{Z}\right)^{10} - 5\left(\frac{\sigma_{LL}}{Z}\right)^4\right\}. \tag{5}$$

Here, Z is the distance from the first ML and σ_M is the equilibrium inter-particle distance in the first ML. The energy valley of $\phi(Z)$ in Eq. (5) is at point Q' with $Z = \sigma_{LL}$, and the valley depth is

$$\varphi(Z)\Big|_{z=\sigma_{LL}} = \frac{4\sqrt{3}\pi}{5}\frac{\varepsilon_{LL}{\sigma_{LL}}^2}{\sigma_M^2}. \tag{6}$$

After calculation, we find that at point Q' the sidewall potential is only about 0.06 of the first ML with σ_M equal to σ_{LL}; then, the influence of the sidewall on the second ML formation can be safely ignored, and the particle density peak of the second ML appears at the distance $Z = \sigma_{LL}$ from the first ML where the potential energy valley of the first ML appears, or equivalently, the second ML thickness is σ_{LL}. We need to point out that one important underlying simplification is that the influences of the second and other MLs on the first ML formation are ignored, which are much weaker than the influence of the pillar sidewall.

Although the position of the second ML particle density peak should be determined by the valley point of the summation of the sidewall potential and the first ML potential, since there is no analytical expression of the sum potential, we use the above method for simplicity. In this way, the influence of the MD parameter on the simulation results is highlighted.

Similarly, the properties of the other MLs would only be determined by the potential field of their previous MLs. Straightforwardly, the total ML thickness is $d_Q + n\sigma_{LL}$, where d_Q is the first ML thickness, σ_{LL} is the thickness of the other MLs, and n is the number of MLs except the first ML, which depends on how we define the ML–vapor interface. No matter where the ML–vapor interface is, $d_Q + n\sigma_{LL}$ (equals to $0.86\sigma_{SL} + n\sigma_{LL}$ and σ_{LL} is fixed during the simulations) only varies with σ_{SL} in our simulations. Then, the total ML would be thicker for larger σ_{SL}, and the escape of the droplet particles at the TPL to the pillar sidewall would be easier, which actually corresponds to a larger κ_0. Eventually, the pinning energy at the pillar edge defect is reduced more significantly. This conclusion is in good accordance with the data in Table 1.

What is more, the ML with larger particle density causes easier particle escape at the TPL, and thus corresponds to a larger κ_0 and larger pinning energy reduction. In the first ML, the particle density is determined by the sidewall potential energy valley depth, which is linearly related to ε_{SL} as indicated in Eq. (3); in the other MLs, the particle densities are directly determined by the potential valley depths of the previous MLs, as discussed above.

The fact is that, when the sidewall potential valley depth is deeper (i.e. larger ε_{SL}), the particle density in the first ML is larger, and then the equilibrium inter-particle distance σ_M in the first ML is smaller. This results in a deeper potential valley of the first ML according to Eq. (6), and then further results in a denser second ML. In the same manner, the overall particle density in the MLs is determined by ε_{SL}, no matter where the ML–vapor interface is defined.

Briefly speaking, when σ_{SL} or ε_{SL} is larger, the interaction between the particles at the TPL and the MLs on the pillar sidewall is stronger. Then, the pinning energy E_P is easily overcome by LJ droplets with a volume smaller than the critical value ignoring the ML effect, which agrees well with the results in Table 1.

3.2. Classical explanation of the ML effect

The critical mechanical balance conditions of the TPL at the pillar edge defect along the x and z directions are constructed by adopting the notion of static contact line

friction[24]:

$$\begin{cases} \gamma_{\rm LV}\sin\theta_{\rm e} = \gamma_{\rm SL} + f_x, \\ \gamma_{\rm LV}\sin\theta_{\rm c} = \gamma_{\rm SL} + f'_x, \end{cases} \quad \begin{cases} \gamma_{\rm LV}\cos\theta_{\rm e} = \gamma_{\rm SV} - f_z, \\ \gamma_{\rm LV}\cos\theta_{\rm c} = \gamma_{\rm SV} - f'_z. \end{cases} \tag{7}$$

Here, f_x and f'_x are the static contact line frictions along the x direction, while f_z and f'_z are the static contact line frictions along the z direction. f_x and f_z are the theoretical values according to the formulating of Gibbs, while f'_x and f'_z are the MD simulation results considering the evaporation effect.

The variations of the TPL static friction along the x and z directions caused by the evaporation effect are

$$\begin{cases} \Delta f_x = f'_x - f_x = \gamma_{\rm LV}\left(\sin\theta_{\rm c} - \sin\theta_{\rm e}\right), \\ \Delta f_z = f'_z - f_z = \gamma_{\rm LV}\left(\cos\theta_{\rm e} - \cos\theta_{\rm c}\right). \end{cases} \tag{8}$$

The total reduction of the TPL static friction Δf is

$$\begin{aligned} \Delta f &= \Delta f_x + \Delta f_z \\ &= \gamma_{\rm LV}\left(\sin\theta_{\rm c} - \sin\theta_{\rm e}\right) + \gamma_{\rm LV}\left(\cos\theta_{\rm e} - \cos\theta_{\rm c}\right). \end{aligned} \tag{9}$$

The results of Δf are listed in Table 2 in units of $\gamma_{\rm LV}$.

Table 2. Total reduction of static contact line friction by MD calculation.

$\sigma_{\rm SL} = 0.9\sigma_{\rm LL}$	$\Delta f(\gamma_{\rm LV})$	$\sigma_{\rm SL} = 0.8\sigma_{\rm LL}$	$\Delta f(\gamma_{\rm LV})$
$\varepsilon_{\rm SL} = 0.50\varepsilon_{\rm LL}$	–0.194	$\varepsilon_{\rm SL} = 0.60\varepsilon_{\rm LL}$	–0.216
$\varepsilon_{\rm SL} = 0.55\varepsilon_{\rm LL}$	–0.203	$\varepsilon_{\rm SL} = 0.65\varepsilon_{\rm LL}$	–0.304
$\varepsilon_{\rm SL} = 0.60\varepsilon_{\rm LL}$	–0.470	$\varepsilon_{\rm SL} = 0.70\varepsilon_{\rm LL}$	–0.332

From the results in Table 2, for the same $\sigma_{\rm SL}$, a larger $\varepsilon_{\rm SL}$ corresponds to a larger absolute value of Δf; for the same $\varepsilon_{\rm SL}$ ($\varepsilon_{\rm SL} = 0.60\varepsilon_{\rm LL}$), a larger $\sigma_{\rm SL}$ results in a larger absolute value of Δf. The total reduction of the pinning energy $\Delta E_{\rm P}$ at the pillar edge consists of two parts: ΔE_x along the x direction, and ΔE_z along the z direction. ΔE_x and ΔE_z are assumed to be the increasing functions of the friction reductions Δf_x and Δf_z, respectively. Then, we know that the large absolute value of Δf (corresponding to a large $\sigma_{\rm SL}$ or $\varepsilon_{\rm SL}$) indicates that the pinning energy barrier reduction $\Delta E_{\rm P}$ is large, which agrees well with the discussion in Subsection 3.1.

4. Conclusions

From the MD simulation of the LJ liquid wetting behaviors at the edge defect of a single stripe pillar, the pre-wetting phenomenon is observed. It is revealed that the existence of the quasi-liquid ML on the pillar sidewall reduces the edge pinning energy barrier, which prevents the droplet from sliding down. The degree of pre-wetting is directly related to the particle interaction parameters, which is explained in both atomic and classical ways. The results in this work are useful to understand the Cassie–Wenzel state transition process on the stripe pillar array at high temperatures when the droplet evaporation–condensation effect should be considered and the existence of the ML on the pillar array sidewalls significantly lowers the Cassie–Wenzel state transition energy barrier.

Acknowledgment

The MD simulations were performed with the DeepComp 7000 computer at the Supercomputer Center of the Computer Network Information Center, Chinese Academy of Sciences.

References

[1] Damle V G and Rykaczewski K 2017 *Appl. Phys. Lett.* **110** 171603
[2] Kwon D, Wooh S, Yoon H and Char K 2018 *Langmuir* **34** 4732
[3] Chen S Y, Kaufman Y, Schrader M A, Seo D, Lee D W, Page S H, Koenig P H, Isaacs S, Gizaw Y and Israelachvili J N 2017 *Langmuir* **33** 10041
[4] Semprebon C, McHale G and Kusumaatmaja H 2017 *Soft Matter* **13** 101
[5] Gao L C and McCarthy T J 2006 *Langmuir* **22** 2966
[6] Wang S T, Liu K S, Yao X and Jiang L 2015 *Chem. Rev.* **115** 8230
[7] Lundgren M, Allan N L and Cosgrove T 2003 *Langmuir* **19** 7127
[8] Patankar N A 2004 *Langmuir* **20** 7097
[9] Extrand C W 2005 *Langmuir* **21** 10370
[10] Wang S and Jiang L 2007 *Adv. Mater.* **19** 3423
[11] Cassie A and Baxter S 1944 *Trans. Faraday Soc.* **40** 546
[12] Wenzel R N 1936 *Ind. Eng. Chem.* **28** 988
[13] Xue Y H, Lv P Y, Lin H and Duan H L 2016 *Appl. Mech. Rev.* **68** 030803
[14] Liu T Q, Li Y J, Li X Q and Sun W 2017 *J. Phys. Chem. C* **121** 9802
[15] Cheng Y T and Rodak D E 2005 *Appl. Phys. Lett.* **86** 144101
[16] Zhang T, Wang J, Chen L, Zhai J, Song Y L and Jiang L 2011 *Angew. Chem. Int. Ed.* **50** 5311
[17] Oliver J F, Huh C and Mason S G 1977 *J. Colloid. Interf. Sci.* **59** 568
[18] Gibbs J 1961 *Scientific Papers* (Dover: Dover Reprint) **Vol. 1** p. 326
[19] Tadmor R 2004 *Langmuir* **20** 7659
[20] Jerison E R, Xu Y, Wilen L A and Dufresne E R 2011 *Phys. Rev. Lett.* **106** 186103
[21] Wang F C and Wu H A 2015 *Sci. Rep.* **5** 17521
[22] Plimpton S 1995 *J. Comp. Phys.* **117** 1
[23] Weijs J H, Marchand A, Andreotti B, Lohse D and Snoeijer J H 2011 *Phys. Fluids.* **23** 022001
[24] Coninck J D and Blake T D 2008 *Annu. Rev. Mater. Res.* **38** 1
[25] Mayama H and Nonomura Y 2011 *Langmuir* **27** 3550
[26] Yuan Q Z and Zhao Y P 2010 *Phys. Rev. Lett.* **104** 246101
[27] Gennes P G 1985 *Rev. Mod. Phys.* **57** 827
[28] Blake T D and Coninck J D 2002 *Adv. Colloid. Interface. Sci.* **96** 21
[29] Maruyama S, Kurashige T, Matsumoto S, Yamaguchi Y and Kimura T 1998 *Nanosc. Microsc. Therm.* **2** 49